Anisotropic optical properties of indium tin oxide thin films prepared by ion beam sputtering under oblique angle deposition

Simon Hurand, Alan Corvisier, Bertrand Lacroix, Antonio Jesús Santos, Florian Maudet, Cyril Dupeyrat, Rafael García Roja, Francisco Miguel Morales, Thierry Girardeau, Fabien Paumier

Version of Record: https://www.sciencedirect.com/science/article/pii/S0169433222005177
Manuscript_ef9a0191581f5c70602fa56242ee4654

Anisotropic optical properties of indium tin oxide thin films prepared by ion beam sputtering under oblique angle deposition

Simon Hurand[a], Alan Corvisier[a], Bertrand Lacroix[b,c], Antonio Jesús Santos[b,c], Florian Maudet[a], Cyril Dupeyrat[a,d], Rafael García Roja[b,c], Francisco Miguel Morales[b,c], Thierry Girardeau[a], Fabien Paumier[a]

[a] *Institut Pprime, UPR 3346 CNRS-Université de Poitiers-ENSMA, 11 boulevard Marie et Pierre Curie, Futuroscope-Chasseneuil Cedex, 86962, France*
[b] *Department of Materials Science and Metallurgic Engineering, and Inorganic Chemistry, Faculty of Sciences, University of Cádiz, Spain*
[c] *IMEYMAT: Institute of Research on Electron Microscopy and Materials of the University of Cádiz, Spain*
[d] *Safran Electronics and Defense, 26 avenue des Hauts de la Chaume, Saint-Benoît, 8696, France*

Abstract

Unraveling the anisotropic optical properties of nanometer-scale structured thin films is of great interest for both fundamental and applicative perspectives, but can be challenging and is therefore generally overlooked, especially for transparent and conducting materials. In this paper, porous slanted columnar thin films of indium tin oxide are prepared under Oblique Angle Deposition (OAD) by Ion Beam Sputtering (IBS) using argon and xenon as process ions. Their anisotropic optical properties are investigated both in the Visible-NIR range (400 nm to 1.7 μm) and the Infrared range (1.7 to 30 μm) by means of Mueller Matrix Spectroscopic Ellipsometry. The optical models and their results are confronted to and confirmed by High Resolution Transmission Electron Microscopy (HRTEM) studies. In the Visible-NIR range, the resulting picture is that of a ripple-like structure with greater optical index in the direction perpendicular to the slanting plane. This configuration is quite original for OAD films, for which the optical index is usually greater in the direction parallel to the columns, and appears to be a specific footprint of IBS due to the enhanced diffusion of the species during deposition. In the Infrared range, the strong optical anisotropy observed for the Xe-deposited films is explained by the anisotropic free-carrier scattering inside the nanoscopic sub-columnar structure evidenced by HRTEM, yielding to a biaxial Drude model. This mechanism is highly original for OAD films, and may be of a great help to elucidate the anisotropic optical properties of other OAD metallic systems, for which such a sub-columnar structure appears to be a general trend. More generally, this work proposes an original and thorough method combining advanced optical modeling and transmission electron microscopy studies to unravel the anisotropic optical properties of nanostructured thin films.

Keywords: Indium tin oxide, Ion Beam Sputtering, Oblique Angle Deposition, Mueller Matrix, Spectroscopic Ellipsometry, Anisotropy

1. Introduction

Understanding the optical anisotropy in thin films is of great interest both from a fundamental point of view, to unravel their often complex interactions with light, and for their applications in photonics to develop new functions such as retarders or high-transmittance polarizers. Optically anisotropic films can be achieved either by depositing materials with intrinsic anisotropic properties (but in this case the optical indexes are constrained by the available materials) or by the nano-engineering of metamaterials through nanometer-scale structuration of isotropic materials. This can be done by introducing anisotropic inhomogeneities within the films by mixing different materials or by simply inducing porous inclusions through processes like standard lithography techniques, sol-gel deposition, chemical etching of heterogeneous thin films, or spin-coating of nanoparticles.

Oblique angle deposition (OAD) is another promising technique to fabricate nanostructured thin films, giving rise to columnar and porous structures thanks to the shadowing effect, with a fine control on the porosity and the anisotropic properties. OAD is of particular interest as it allows large-scale production by standard physical vapor deposition methods, without the need of any lithographic step, and is therefore directly applica-

ble to established industrial processes. The versatility of this technique make it suitable for the deposition of a variety of materials. By depositing a dielectric material, it allows achieving films with reduced optical indexes of great interest for the manufacturing of high-performance antireflective coatings [1, 2, 3], as well as promoting optical anisotropy due to the slanted columnar structure [4].

In this paper, the anisotropic optical properties of indium tin oxide (ITO) films prepared by OAD will be the central aim. ITO is widely used as a transparent and conductive coating for numerous applications such as liquid-crystal displays [5, 6, 7], light-emitting devices [8, 9, 10], solar cells [11, 12, 13], electrochromic devices [14], de-icer [15], anti-reflective and anti-static tube coatings [16], transparent thin film transistors [17], electromagnetic or heat shieldings [18, 19, 11], electrochromic devices [20], or electro-optic modulators [21], thanks to its unique performances, such as the fine-tuning of the onset of free carrier absorption through the doping level and its unrivaled figure of merit (linked to the ratio of optical over electrical conductance) in the visible range [22, 23]. Nanostructuration has also been used to produce ITO surfaces with improved or new optical properties. For instance, it was shown that the formation of ITO nanorods arrays based on lithography processes gives rise to a tunable plasmon edge and anisotropic optical properties [24]. OAD has also often been considered in the literature, to enhance the transparency in the near-infrared range (NIR) where free carrier absorption prevails [25], to engineer optical retarders through optical anisotropy development [26], and to promote multiple localized surface plasmon resonances in disordered nanostructure for radiative cooling applications [27].

Most of the studies related to OAD fabrication of ITO films have focused on evaporation processes [26, 28, 29, 30, 13], which produce highly porous columnar films but with little control on the crystallinity and the doping of ITO. Also, the anisotropic optical properties of those films are generally overlooked, or not thoroughly studied, because of the difficulty to characterize them, so that exploring this facet is still necessary. In a previous work [25], it was shown that OAD combined with ion beam sputtering (IBS) deposition can be used to fabricate crystalline ITO films with controlled nanostructure and tunable optical properties. IBS consists in a bombardment of an ITO target by an incident ion that can be chosen appropriately, such as argon or xenon [31, 32]. This technique produces crystalline films by deposition at room temperature, which is a frequent bottleneck for large-scale industrial applications onto various electro-optical components such as complex heterostructures for solar harvesting [13], radiative cooling [27], or sensors. The crystallinity, the electron doping and the porosity can be further tuned adequately by the choice of the impinging ion [25], and by the scattering angle of the primary ions, which is a typical flexibility of IBS deposition compared to e.g. Magnetron Sputtering [33], opening a wide range of film properties.

In the continuity of this work, in which the relation between the nanostructure and the isotropic optical properties of OAD ITO films grown by IBS has been thoroughly addressed [25], the present paper now focuses on the study of their optical anisotropy by means of Mueller Matrix Spectroscopic Ellipsometry (MM SE) from the visible to the infrared range, and on the development of adequate optical models relying on results obtained at the nanoscale by high-resolution transmission electron microscopy. This study will contribute to fill the current knowledge gap of these systems by providing a deeper understanding of the optical properties of nanostructured and anisotropic ITO thin films, which is of great interest for the scientific community and for numerous applications, and transposable to other metallic OAD films.

2. Methods

2.1. Ion beam sputtering deposition at oblique angles

Tin doped indium oxide nanostructured films were fabricated at room temperature on silicon substrates by ion beam sputtering deposition in a Nordiko chamber which includes two radio-frequency sources. The primary source was used to produce Ar or Xe ions accelerated at 1.2 keV with a current of 80 mA to sputter a 15-cm-diameter water-cooled sintered ceramic target of ITO containing a nominal concentration of 10 wt. % SnO_2 and inclined by an angle of 45 ° relative to the primary ion flux. During the process, oxygen was introduced in the chamber through an assistance gun with a flow of 5 sccm. Oblique deposition was performed by placing the substrates on a laboratory-made substrate holder specially designed to allow the growth at different angles α from 50 to 85 ° (α represents the angle between the substrate normal and the incident vapor flux) with a step of 5 ° for a duration of 2 hours without interruption.

2.2. Morphological, structural and compositional analyses

After deposition, the general cross-sectional or top-view morphologies of the films were studied by Scan-

ning Electron Microscopy (SEM) in secondary electron imaging mode using a field emission gun 7001F-TTLS (JEOL Co. Inc.) microscope at an accelerating voltage of 20 kV. Transmission Electron Microscopy (TEM) experiments (Bright Field (BF) and High Resolution (HR) TEM imaging) were conducted in two microscopes operated at 200 kV (JEOL 2100 and JEOL 2010F). High-Angle Annular Dark-Field imaging (HAADF) was also carried out using the Scanning TEM (STEM) mode.

Cross-sections lamellae for TEM observations within the slanting plane of the columns were prepared by mechanical polishing using a tripod apparatus up to less than 10 μm followed by Ar ion milling in a GATAN PIPS system (3.5 keV, $\pm 7^\circ$ incidence). To minimize irradiation damage, the final step was performed at 2.5 keV, $\pm 5^\circ$ during 5 min up to electron transparency. Additionally, TEM cross-sections for observation in the direction perpendicular to the previous one and with the columns tilted at their slanting angle were prepared by Focused Ion Beam (FIB) using a ZEISS Crossbeam 550 FIB-SEM system. Before insertion into the column of the TEM microscope, the prepared samples lamellae were cleaned in a plasma cleaner to remove residual hydrocarbon contamination.

2.3. Optical characterizations

All ITO films deposited on silicon were characterized by Mueller Matrix Spectroscopic Ellipsometry (MM SE) to obtain the Mueller Matrix (MM) elements. These analyses were carried out in the visible to near-infrared range (Visible-NIR) from 400 nm to 1.7 μm using a M2000XI ellipsometer (J. A. Woollam Co. Inc.). Regarding the acquisition parameters, the incidence angle varied form 55 to 80° with a step of 5° and the azimuthal angle was rotated from 0 to 180° by a step of 15°. Complementary analyses were performed in the infrared (IR) range from 1.7 to 30 μm using a Vase-IR Mark II ellipsometer (J. A. Woollam Co. Inc.). The acquisition parameters in the IR range were identical to those used for the Visible-NIR range. Both M2000XI and Vase-IR Mark II are Rotating Compensator (RC) ellipsometers comprising a single RC, which allow the measurement of 12 out of the 16 MM elements: the first 3 rows/columns for the M2000XI/Vase-IR Mark II, respectively, because the RC is placed at the entry/exit arm, enabling the measurement/emission of all but circular light, so that the last row/column of the Mueller Matrix is missing. The modeling was performed with the CompleteEASE software developped by the J. A. Woollam company.

3. Nanostructure

Due to the strong diffusion of the species on the substrate arising from the impinging ion, IBS OAD ITO films typically exhibit a two-layer structure, as we evidenced in a previous work [25]. A first ITO layer, which is completely dense, appears close to the substrate. On top of it grows a second layer, which is porous and with a slanted columnar structure arising from the oblique angle deposition. Upon increase of the deposition angle α, the porosity, the thickness and the slanting angle of the second layer increase continuously, as commonly observed for OAD by various processes [29, 34]. Interestingly, while the thickness of the first layer typically decreases with α, it never completely disappears, remaining as a thin, dense underlayer of a few tens of nanometers even at high α. This property appears to be a singular feature of IBS deposition.

Regarding the optical properties, this first seed layer with islands grown on the substrate usually make it quite challenging to perform optical modeling by effective-medium approaches, simply because this seed layer is much denser than the porous nanostructure growing over it. In our previous work [25], we evidenced that it is possible to successfully tackle this challenge by splitting the ITO films into two layers in the optical modeling: the first layer is comprised solely of ITO, whereas the second layer is comprised of ITO plus air as porous inclusions. The results of this analysis has been thoroughly compared with the microstructure observed by TEM on the same films, and a very nice agreement has been found. The optical indexes of ITO inside the two layers are found to be similar in the visible range, but different in the near-infrared range (NIR) close to the plasma frequency due to different electron doping levels. The first dense layer typically exhibits higher free electron concentration than the second porous one, which is attributed to a higher degree of crystallinity clearly identified by transmission electron microscopy. What is more, Xe films (i.e., deposited with xenon as the sputtering ions) have a generally higher crystallinity and higher electron concentration than the Ar ones, which is linked to the higher bombardment rate by the lighter Ar ions.

In this work, we investigate the anisotropic optical properties of these films. To gain further insight into the microstructure of the columnar films, we perform scanning electron microscopy (SEM) and Transmission Electron Microscopy (TEM) with various cross-sectional views and different inclinations. Figure 1 shows cross-sectional views by High Angle Annular Dark Field scanning TEM (STEM-HAADF) of an IBS

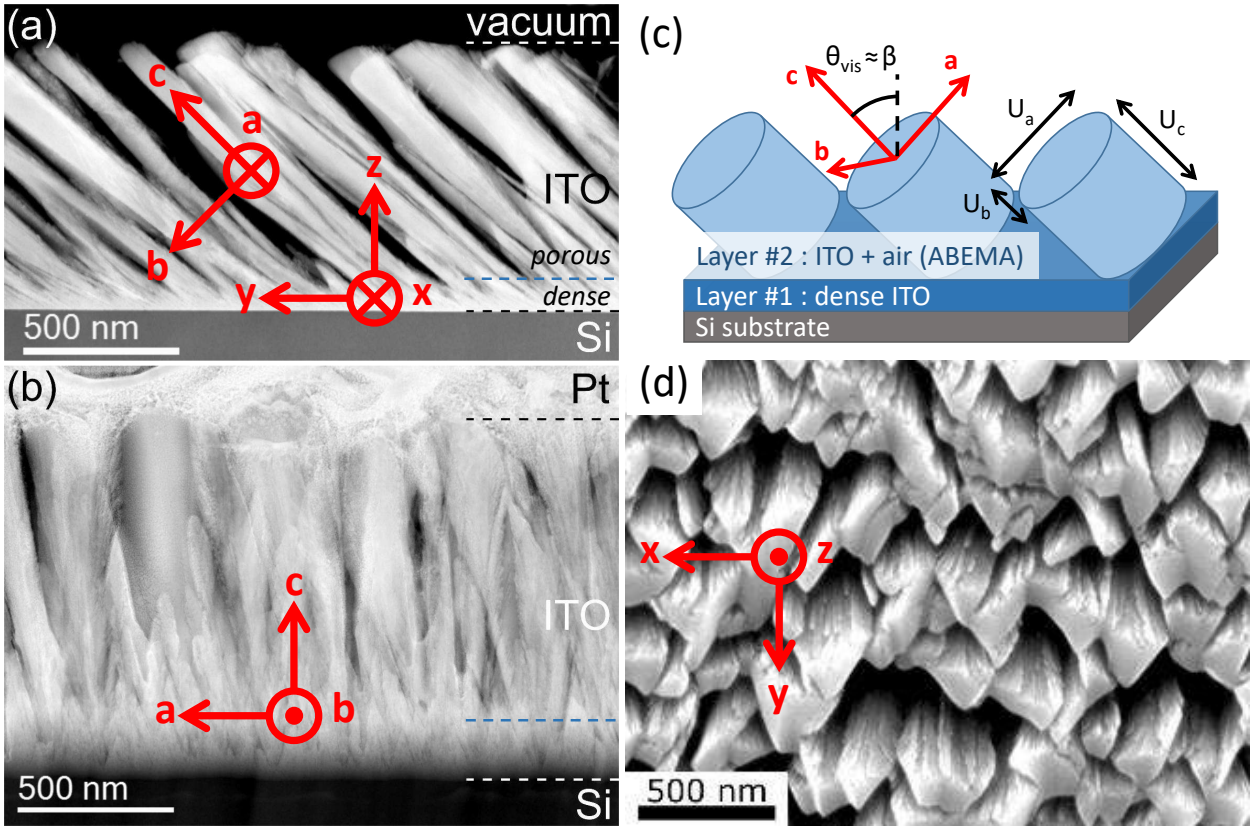

Figure 1: STEM-HAADF micrographs of cross-sectional views (a) within the slanting plane of the columns, (b) in the direction perpendicular to the previous one and tilted at the column slanting angle of 56 ° (the Platinium (Pt) overlayer stems from the slicing process by FIB), and (d) top-view SEM micrograph of an Xe IBS OAD ITO film elaborated with a deposition angle $\alpha = 85\,^{\circ}$. The blue dashed line indicates the limit between the dense (Layer #1) and porous (Layer #2) layers. (c) Schematic of the optical model for the Visible-NIR range.

film deposited at $\alpha = 85\,^{\circ}$ oblique angle with xenon as the impinging ion. Cross-sectional view within the slanting plane of the columns (Figure 1(a)) evidences the persistence of a thin dense underlayer even at such high α. On the other hand, cross-sectional view in the plane which is inclined at the column slanting angle of 56 °, containing the direction c of the columns and the direction x perpendicular to the slanting plane (Figure 1(b)), evidences short, dead-end columns close to substrate, substituted further from it by wide and fanning columns, that finally get connected to one another. This strong lateral connection is also visible from the top-view SEM micrograph (Figure 1(d)). Therefore, the porous and slanted second layer can be pictured as a ripple-like structure in the direction x perpendicular to the slanting plane, with almost continuous walls of ITO. Their thickness in the direction b within the slanting plane is typically of the order of 100 nm.

4. Optical properties

4.1. Visible-NIR range

In the Visible-NIR range (400 nm to 1.7 μm), ITO behaves as a dielectric. The analysis of the Mueller Matrix (MM) elements measured by Mueller Matrix Spectroscopic Ellipsometry (MM SE) for both Ar- and Xe-deposited ITO films evidences two pseudo-isotropic directions for the azimuthal angles $\phi = 0\,^{\circ}$ and $180\,^{\circ}$, corresponding to the plane of incidence being parallel to the slanting plane of the columns. For an angle ϕ different than $0\,^{\circ}$ or $180\,^{\circ}$, the MM elements of all ITO films exhibit no particular symmetry (Fig. 2). These observations indicate an orthorhombic biaxial structure, with the principal axis pointing at an inclined angle in the slanting plane of the columns [35, 36]. Taking into account the two-layer structure of our films, we therefore model the optical properties with a two-layer model, as

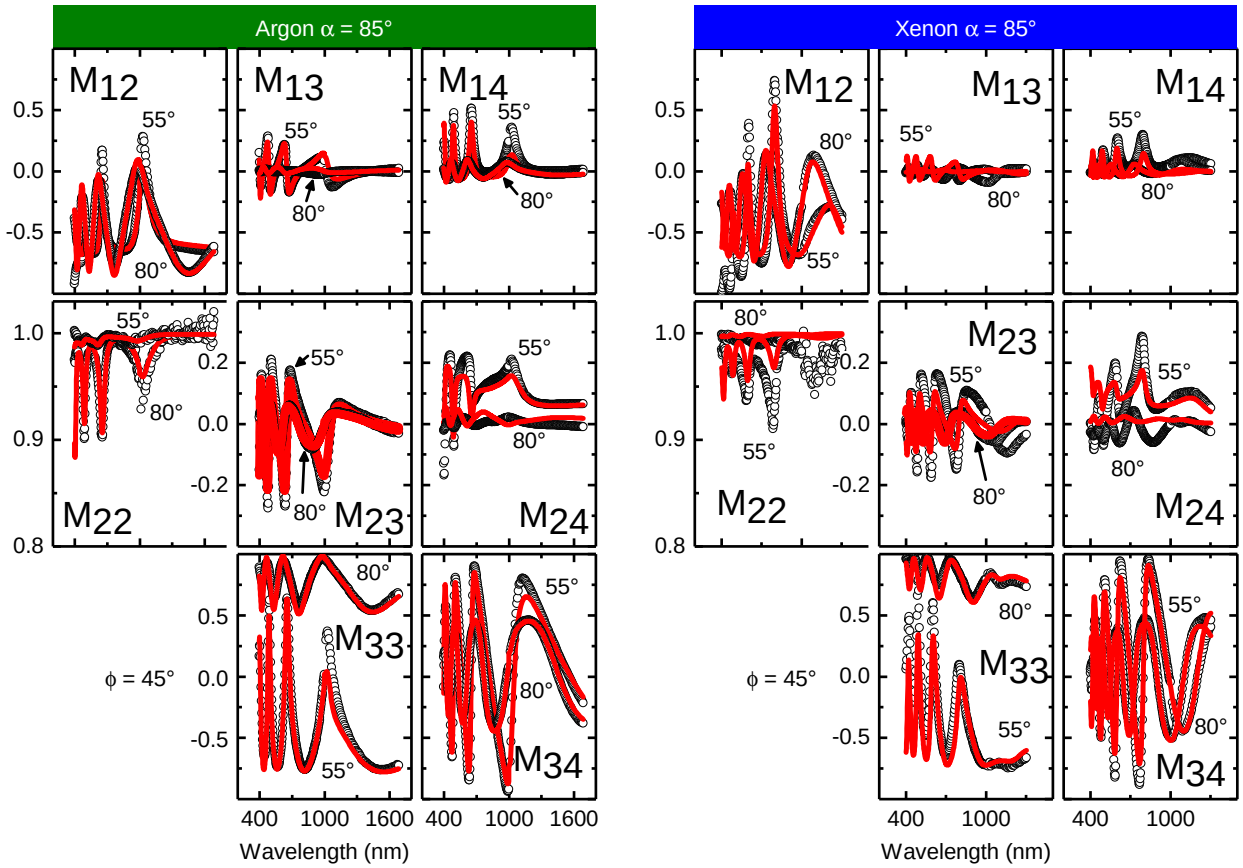

Figure 2: Experimental (black) and best-fit (red) MM elements as a function of the wavelength in the Visible-NIR range, for an azimuthal angle $\phi = 45\,^\circ$ and for incidence angles of 55 and 80 °, for Ar (left column) and Xe (right column) IBS OAD ITO films deposited at $\alpha = 85\,^\circ$.

frequently done for ITO films [37], which is schematized in Figure 1(c). The first layer, at the bottom of the ITO film, close to the substrate, is dense and isotropic. The second layer, on top of the first one, is biaxial and can be potentially porous.

The optical properties of the dense ITO within each layer were reproduced using a three-oscillators model: (i) a Tauc-Lorentz Oscillator (TLO) with an energy gap close to 3.5 eV ($\lambda_{\text{gap}} \approx 360$ nm) modeling the direct band gap absorption of ITO; (ii) a Gaussian oscillator (GO) arbitrarily centered out of the measurement range at 8 eV to model the UV interband transitions and the resulting dispersion in the visible range; (iii) a Drude oscillator (DO) modeling the free-carrier plasma excitation in the NIR range. The complex dielectric function $\varepsilon(\omega)$ of ITO as a function of the frequency ω thus reads:

$$\varepsilon(\omega) = \varepsilon_\infty + \varepsilon_{\text{GO}}(\omega) + \varepsilon_{\text{TLO}}(\omega) + \varepsilon_{\text{DO}}(\omega) \qquad (1)$$

Where ε_∞ is an infinite-frequency dielectric constant reproducing the interband transitions further in the UV. The explicit mathematical expressions of the dielectric function of each oscillator are given in the supplementary material. The parameters for the TLO, GO and ε_∞ are kept the same for the two layers, and also for all the deposition angles for each type of impinging ion (Ar or Xe). Only the DO parameters are allowed to be different for layer 1 or 2, with free electron densities N_{e1}, N_{e2} and mobilities μ_1, μ_2. The details of the model, as well as the evolution of its parameters with respect to the deposition angle α, are given in Ref. [25]. When the second layer is biaxial and porous, which is the case for $\alpha \geq 55\,^\circ$ for both Ar and Xe films, its biaxial behavior is accounted for in the framework of the Anisotropic Bruggeman Effective Medium Approximation (ABEMA) [38]. In this model, the shape of the inclusion is elliptical, with shape parameters U_j ($j = a, b, c$), giving rise to the depolarization factors L_j as follows [39, 40, 41]:

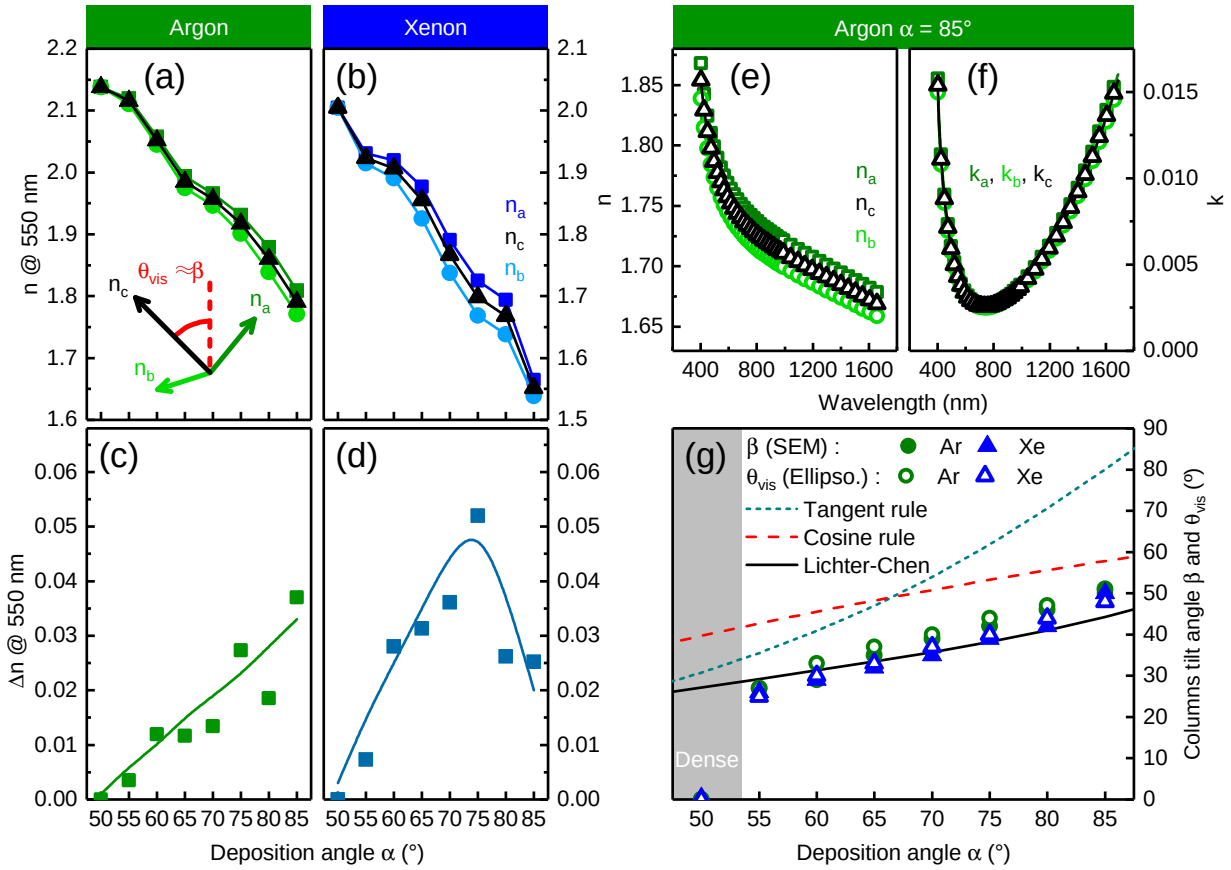

Figure 3: Results of the optical modeling in the Visible-NIR range. (a) Optical indexes n_a, n_b, n_c for Ar and (b) for Xe of the second layer of the IBS OAD ITO films at the wavelength of 550 nm depending on the deposition angle α, and the corresponding in-plane birefringence Δn (c) for Ar and (d) for Xe (the solid lines are guides to the eye). (e) Real part n and (f) imaginary part k of the optical indexes in the three directions a, b, c as a function of the wavelength, for the film deposited with argon ions at an incidence angle of $\alpha = 85\,^\circ$. (g) Columns tilt angles of Ar (green) and Xe (blue) films, as measured by SEM (β, full symbols) or extracted from spectroscopic ellipsometry analysis (θ_{vis}, open symbols). Theoretical tendency predicted by cosine rule, tangent rule, or Lichter-Chen rule with a fitting parameter $\Phi = 0.6$, are also displayed for comparison.

$$L_j = \frac{U_a U_b U_c}{2} \int_0^\infty \frac{(s + U_j^2)^{-1} \mathrm{d}s}{\sqrt{(s + U_a^2)(s + U_b^2)(s + U_c^2)}} \quad (2)$$

The effective dielectric constant $\varepsilon_{\text{eff},j}$ in the j-th direction is then determined as a function of the dielectric constants $\varepsilon_{n,j}$ and the volumic fractions f_n of each of the two media n, namely, ITO and the air filling the porosities, thanks to the Bruggeman formula [42, 39]:

$$\sum_{n=\text{ITO,air}} f_n \frac{\varepsilon_{n,j} - \varepsilon_{\text{eff},j}}{\varepsilon_{\text{eff},j} + L_j(\varepsilon_{n,j} - \varepsilon_{\text{eff},j})} = 0 \quad (3)$$

The biaxial structure implies further rotations with the Euler angles φ_{vis}, θ_{vis} and ψ_{vis}, to describe the orientation of the principal axis a, b, c with respect to the Cartesian frame x, y, z of the sample.

By fitting our model onto the measured MM elements, we extract the relevant parameters for all the films. Selected measured elements of the Mueller matrices, together with the resulting best-fit model, are displayed in Figure 2 for an azimuthal angle of $\phi = 45\,^\circ$ for which the off-diagonal elements are maximum. The results of the optical modeling in the Visible-NIR range are shown in Figure 3.

The Euler angle φ_{vis} resulting from the fit procedure is found to be very close to zero for all the measured samples, consistently with the two pseudo-isotropic directions observed for $\phi = 0$ and $180\,^\circ$. The inclination θ_{vis} of the principal axis c is found to correspond to the slanting angle β of the columns measured by SEM, as displayed in Figure 3(g). As expected, the tilt angle β of the nanocolumns relative to the substrate normal increases with α. However, common empirical ballistic

approaches such as the tangent rule [43] and Tait's rule [44] fail in describing correctly the experimental evolution and magnitude of β versus α. A better description of the β values is actually found with the Lichter and Chen expression [45] using a parameter $\Phi = 0.6$, which points out a diffusivity and deposition rate dependence, as we already discussed in Ref. [25]. Lastly, the existence of two pseudo-isotropic directions for $\phi = 0$ and $180\,^\circ$ is only possible if one of the optical axis is perpendicular to the plane of incidence in these positions [36]. This means that the last Euler angle ψ_{vis} has to be zero, meaning that the a axis is perpendicular to the slanting plane, identical to the x-direction of the ripples observed by TEM. Such inclined biaxial properties are very similar to that reported for OAD films, see e.g. Ref. [46, 36].

The wavelength dependence of the real part n of the optical indexes in the three directions a, b, c of the second (porous) layer is displayed in Figure 3(e) for the film deposited with argon ions at an incidence angle of $\alpha = 85\,^\circ$ as a representative example: for all the other samples deposited at other α angles and/or with xenon ions, the n and k variations versus wavelength are very similar, with a simple upwards or downwards overall shift, that is displayed in Figure 3(a) and (b), due to the change in porosity. As one can see, the optical index n_a (in the direction of the ripples) is steadily higher than n_c (parallel to the columns) on all the wavelength range, and n_b is steadily the smallest one. This ordering is maintained for all the Ar and Xe samples, as can be seen on the Figure 3(a) and (b), respectively, where the optical indexes n_a, n_b, n_c are plotted at a single wavelength of 550 nm. Regarding the imaginary part $k_{a,b,c}$, as displayed in Figure 3(f), it remains very small in the visible range for all three directions a, b, c, while an uprise takes place on the UV and the NIR sides due to the interband and intraband (i.e. free-carrier-driven) transitions, respectively.

This ordering ($n_a > n_c$) is quite surprising, as OAD films commonly deposited by electron beam evaporation such as SiO_2 [46] or Co, Ti and Si [36] usually exhibit $n_c > n_a$, which is due to the elongated shape of the columns in the c direction. To gain further insight into this surprising result, we analyzed the TEM micrographs taken along three different view points displayed on Figure 1(a), (b) and (c), and we extract the typical widths of the nanocolumns in the three different directions a ($\sim$ 200 nm), b ($\sim$ 100 nm) and c ($\sim$ 1000 nm), which are summarized on Table 1. While the individual columns appears thinner in the a than in the c direction, the TEM micrographs of Figure 1(b) and (c) however also evidence a strong lateral connection between neighboring columns in the a direction, so that the light polarized along this direction experiences uninterrupted travel through a continuous medium (either ITO or vacuum) on a longer length scale, typically of the order of $\sim$ 1000 nm (see Figure 1(b) and (c)), and thus an enhanced optical index. This strong lateral connection appears as a footprint of IBS OAD films, whereas most previous reports focused on ITO OAD films grown by electron beam evaporation [26, 28, 47]. On the other hand, the optical index in the third direction n_b (within the slanting plane but perpendicular to the columns) is always smaller than n_a and n_c, which is consistent with the smaller size of the columns ($\sim$ 100 nm) in this direction.

Optical model				TEM (see Fig. 1)
L_a	0.30	U_a	1600	$\sim$ 200 nm
				+ columns connections
L_b	0.37	U_b	100	$\sim$ 100 nm
L_c	0.33	U_c	1000	$\sim$ 1000 nm

Table 1: Depolarization factors L_a, L_b and L_c and shape parameters U_a, U_b and U_c of the ellipsoidal inclusions (arbitrarily normalized to $U_c = 1000$) obtained from MM SE with the ABEMA optical model for the sample deposited at $\alpha = 85\,^\circ$ with Ar ions, and its comparison to the typical dimensions of the columns as observed by TEM in Fig. 1(a) and (b).

In order to compare the results of the optical modeling with those of the TEM study, the depolarization factors resulting from the optical modeling and the elliptical shape parameters calculated by the mean of formula 2 are also displayed on Table 1 for the sample deposited at $\alpha = 85\,^\circ$ with Ar ions. As the ABEMA model only considers the ratio between U_a, U_b and U_c and not their absolute values, U_c is arbitrarily set to 1000 for the sake of comparison with the TEM values. Although these parameters should not be compared directly in term of magnitude, as detailed for example in Ref. [48, 36], the agreement is striking, given the fact that strong lateral connections exist between neighboring columns in the a direction. The resulting picture is that of a ripple-like structure of the nanocolumns, with a strong elongation along their axis, strong connections in the direction perpendicular to the slanting plane, and reduced dimension in the third direction, which reproduces well the optical properties as well as the nanostructure of the film.

Regarding the anisotropy $\Delta n = n_x - n_y$ in the plane $x - y$ of the film, which is the one relevant for any practical application, it is computed by projection onto the $x - y$ plane, i.e. by taking [49] $n_y = n_b n_c / \sqrt{n_b^2 \sin^2\beta + n_c^2 \cos^2\theta_{\text{vis}}}$, where θ_{vis} is the tilt angle of the columns, and $n_x = n_a$. The values of Δn

are reported in Figure 3(c) and (d) for the Ar and Xe films, respectively. For the Xe films, Δn increases continuously with the deposition angle α up to a maximum of $\Delta_{n,\mathrm{max,Xe}} = 0.05$ at $\alpha = 75\,^\circ$ (Fig. 3(d)). This is commonly explained by the increasing porosity and the increasing asymmetry of the inclusions [49]. At $\alpha > 75\,^\circ$, Δn experiments a downturn. Indeed, the porosity reaches high values, up to 50 %, which reduces dramatically the optical index, and hence the optical indexes difference Δn as it is an absolute value and not a relative one. Such a downturn of Δn at high angle has been commonly reported experimentally [49, 26, 50, 51, 52] and explained theoretically [53, 54, 55] for OAD thin dielectric films. For the Ar films (Fig. 3(c)), surprisingly, no downturn is visible, and Δn keeps increasing up to its maximum value of $\Delta n_{\mathrm{max,Ar}} = 0.04$ at $\alpha = 85\,^\circ$. This observation is quite uncommon for OAD thin films. However, we have shown that Ar films are significantly less porous than the Xe ones [25], which is also clearly visible through the higher values of the optical indexes n_a, n_b and n_c reported in Figure 3. Therefore, it is possible that the porosity is not sufficient to provoke a downturn of Δn even at high incident angle. The fact that the maximum value $\Delta n_{\mathrm{max,Ar}} = 0.04$ for Ar never reaches the one for Xe $\Delta n_{\mathrm{max,Xe}} = 0.05$ is also a confirmation of this scenario. As a consequence, by choosing appropriately the impinging ion, we are able to modify the shape of the $\Delta n(\alpha)$ curve, overcoming the limitation of the downturn usually observed for OAD films. This appears as a specific flexibility of IBS films, on the contrary to other deposition techniques for which this downturn is always observed [49, 26, 50, 51, 52]. For IBS indeed, not only the incident angle but also the choice of the impinging ion has impact on the porosity of the film. The Δn_{max} values thus obtained are in the range of previously reported OAD ITO films [26] or other OAD dielectric films [49, 26, 50, 51, 52], as well as many common anisotropic materials, such as quartz ($\Delta n = 0.009$), MgF2 ($\Delta n = 0.006$), calcite ($\Delta n = 0.172$) or tourmaline ($\Delta n = 0.03$), making IBS OAD ITO films suitable for practical applications.

4.2. Infrared range

We then investigate the optical properties of the ITO films by Mueller Matrix Spectroscopic Ellipsometry (MM SE) in the infrared range (IR). The measured MM elements and the corresponding best fits are displayed in Figure 4.

We first discuss the case of the Ar films. Surprisingly, for these films, the off-diagonal MM elements measured in the IR range appear to be close to zero, as it can be seen on the second column of Figure 4, indicating a quasi isotropic, or pseudo-isotropic, behavior. This observation is in sharp contrast with the anisotropy observed in the visible range. However, if we model the ITO top layer of these Ar films with the very same model as the one used for the visible range, we obtain a very nice agreement between calculated and measured MM elements, including the fact that the off-diagonal elements are close to zero, as can be seen in Figure 4 for the sample deposited with Ar at $\alpha = 85\,^\circ$, taken as a representative example. This indicates that the level of porosity is too weak (with a maximum value of 30 % for $\alpha = 85\,^\circ$) to induce noticeable anisotropy in the IR range, where the Drude oscillator dominates the optical properties. So to say, the Ar films behave as an almost flat metallic surface in the IR range, despite comprising porous anisotropic inclusions inside them.

We now discuss the case of the Xe films. On the contrary to the Ar films, they display huge non-zero off-diagonal MM elements, with the amplitude of M_{13}, M_{23}, M_{41} and M_{42} reaching values up to 0.3, as can be seen on the last column of Figure 4. That is, these films are highly anisotropic in the IR range. The same two pseudo-isotropic directions as for the visible range can be identified, with no specific symmetry out of these axis, here again leading to a biaxial structure inclined within the slanting plane of the columns.

The optical properties of OAD thin films made of a metallic material are usually modeled by effective medium approximation such as the ABEMA one, that is, exactly the same model as the one used here for the Visible-NIR range, with the only difference that the optical indexes are now typical of a metal (strong n and k modeled e.g. by a Drude oscillator) and not of a transparent material (low n, negligible k). This approach has been developed and applied successfully by Schmidt et al. [36] to Titanium, Cobalt and Silicon films deposited by OAD.

However, in our case, using the same ABEMA optical model as the one used in the Visible-NIR range fails in reproducing the off-diagonal MM elements: in particular, the off-diagonal M_{13}, M_{23}, M_{41} and M_{42} elements are predicted with an amplitude reaching at the most 0.05, at least 6 times smaller than the measured ones (up to 0.3). This means that the elongated shape of the porous inclusions cannot explain the observed anisotropy in the IR range. In Ref. [36], electron-beam evaporation was used with a high $\alpha = 85\,^\circ$ deposition angle, which results in a rather high void fraction of more than 70 %. The path length of the light within the film is therefore much longer than in our films, where the void fraction does not exceed 50 % for the Xe films.

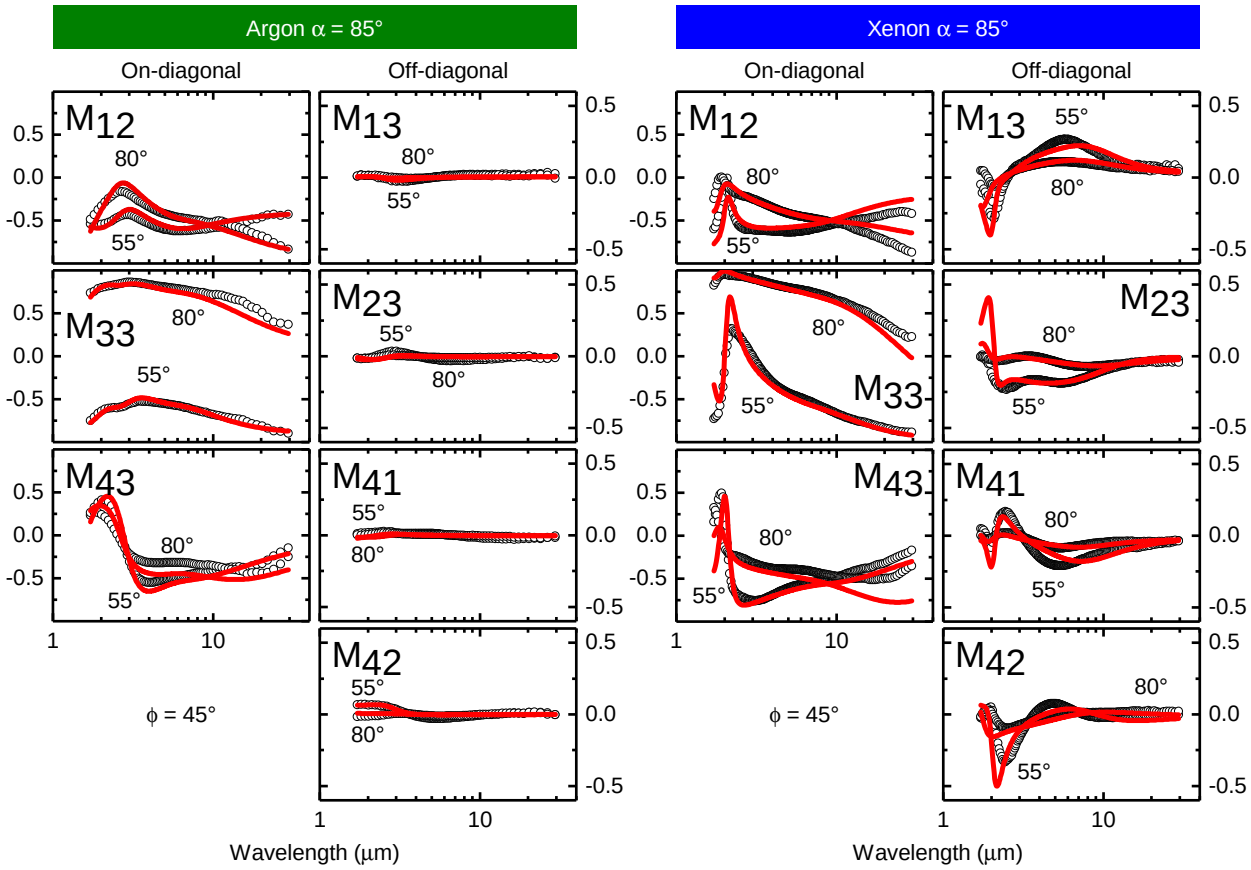

Figure 4: Experimental (black) and best-fit (red) MM elements at an azimuthal angle of $\phi = 45^\circ$ depending on the wavelength and for incidence angles of 55 and 80° in the IR range of Ar (left column) and Xe (right column) IBS OAD ITO films deposited at $\alpha = 85^\circ$. On-diagonal MM elements M_{12}, M_{22}, M_{33} and M_{43} are plotted on the left column, and off-diagonal ones M_{13}, M_{23}, M_{41} and M_{42} on the right column for each sample.

For such an intermediate level of porosity, EMA-based approaches are indeed known to provide poor agreement with experimental data for metal-dielectric mixtures [56, 4]. It thus appears that the path length is not long enough to reveal the anisotropy due to the porous inclusions within the film. On the contrary, the observed anisotropy is linked to the intrinsic properties of the ITO within the columns at the very top of the film.

Sometimes, OAD metallic films can also reveal a monoclinic behaviour of their optical constants [4, 57]. However, attempts to add monoclinicity to an ABEMA model also fails in reproducing the observed anisotropy of our films. Since monoclinicity is believed to stem from charge transfer at the bottom (wetting) nucleation layer of the film [58, 57], it is understandable that this cannot be observed in our ITO films, since the light actually never reaches the bottom layer in the IR range due to the reduced path length, as already pointed out by Mansour et al. for low-porosity Chromium OAD films [59].

Therefore, another optical model should be drawn for the IR range for Xe films. The second (top) layer of the film is modeled as a biaxial material, in which the ITO has three different Drude oscillators for the a, b and c directions, inclined with the Euler angles θ_{IR}, φ_{IR} and ψ_{IR}. We note that $\varphi_{\mathrm{IR}} = 0$ and $\psi_{\mathrm{IR}} = 0$ for all samples, given the observed pseudo-isotropic directions. Within each axis a, b and c, we further introduce the porosity (identical to the averaged one in the visible range) thanks to an isotropic Bruggeman EMA (BEMA). The carrier density N_e is assumed to be the same for the three Drude oscillators, and only the mobilities are allowed to differ. The Drude contribution to the dielectric functions is thus given by:

$$\varepsilon_{\mathrm{Drude},j} = -\frac{\omega_{\mathrm{P}}^2}{\omega^2 + i\omega/\tau_j} \qquad (4)$$

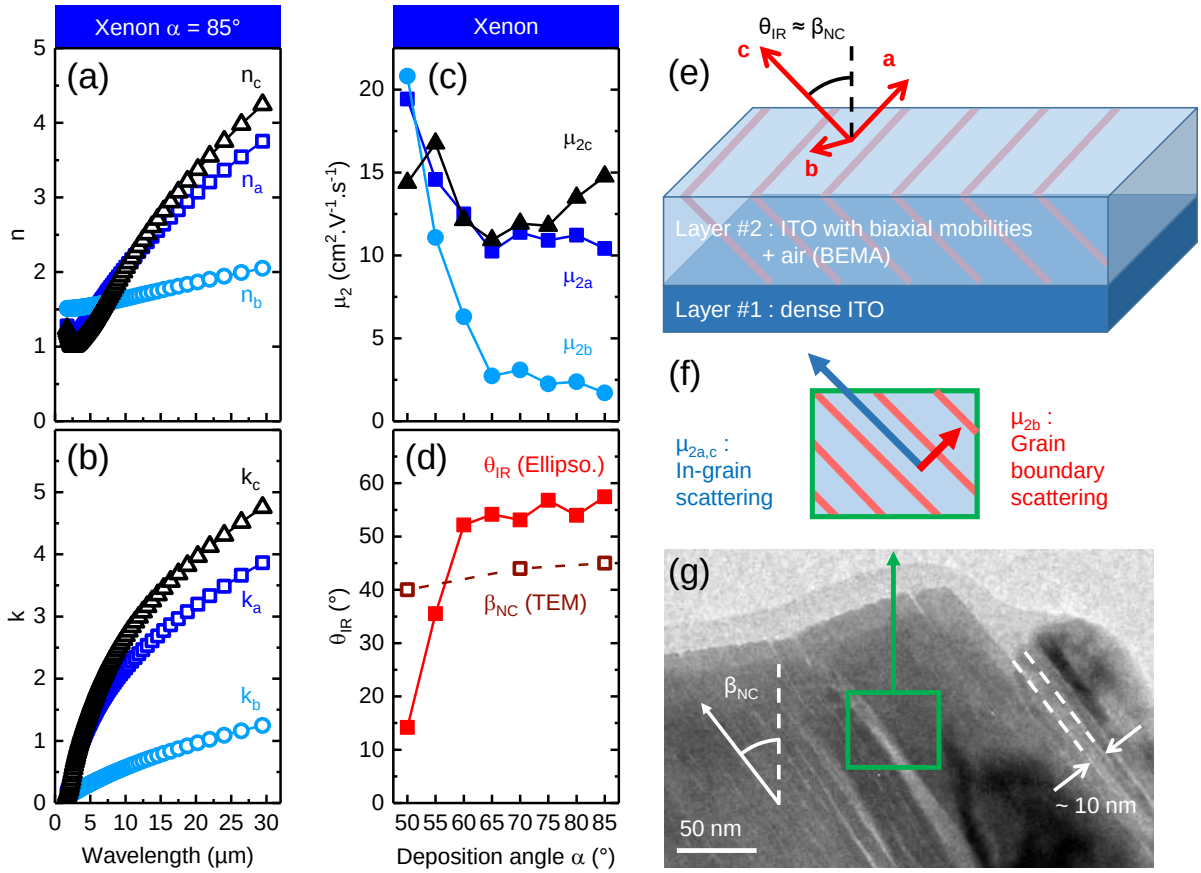

Figure 5: Results of the optical modeling for the Xe films in the infrared range. (a) Real part n and (b) imaginary part k of the optical indexes in the three directions a, b, c as a function of the wavelength, for the film deposited with xenon ions at an incidence angle of $\alpha = 85\,°$. (c) Mobilities in the a, b and c directions and (d) angle of the optical anisotropy in the IR θ_{IR}, plotted together with the tilt angle of the nanocolumns β_{NC} measured by TEM, as a function of the deposition angle α. (e) Schematic of the optical model for the IR range. (f) Schematic of the anisotropic scattering phenomena. (g) Bright field TEM view of the sample deposited with xenon ions at an incidence angle of $\alpha = 70\,°$, illustrating the nanocolumns structure.

Where $\omega_P = \sqrt{\frac{N_e e^2}{\varepsilon_0 m_* m_e}}$ is the unscreened plasma frequency for a carrier density N_e, m_* is the electron relative effective mass and m_e the bare electron mass, ε_0 is the dielectric constant of vacuum and e the elementary charge. Here τ_j is the scattering time that is related to the mobility $\mu_j = \frac{e\tau_j}{m_*}$ along the $j-$th direction ($j = a, b, c$).

The resulting model provides good agreement with the measured MM elements, as can be seen in Figure 4, and the resulting parameters are shown in Figure 5(e) and (f). Several observations can be made thereof. For low deposition angles α, the film is found to be almost isotropic, as the three mobilities μ_{2a}, μ_{2b} and μ_{2c} converge to very similar values. As soon as $\alpha \geq 60\,°$ however, θ_{IR} converges towards a value that is constant with α, close to $\theta_{IR} = 54\,°$. This is surprising, as the inclination of the columns keeps on increasing with α: we note that θ_{IR} differs from the tilt angle of the columns β, which is also close to the optical anisotropy angle θ_{vis} in the visible range. Therefore, for $\alpha \geq 60\,°$, the resulting picture is that of an almost uniaxial structure for the optical properties in the IR range, with a mobility in the a and c directions $\mu_{2a,c} \approx 12\,\mathrm{cm^2.V^{-1}.s^{-1}}$ similar to one another, and to the one derived with an isotropic model $\mu_2 \approx 14\,\mathrm{cm^2.V^{-1}.s^{-1}}$ in Ref. [25], while the mobility in the b direction $\mu_{2b} \approx 3\,\mathrm{cm^2.V^{-1}.s^{-1}}$ is significantly smaller by a factor of 4.

To provide physical insight to the observed anisotropy, one should keep in mind that, in the IR range, the dielectric properties are dominated by the free-carrier absorption edge which is modeled by a Drude oscillator. In this case, the incoming light is mostly reflected, with a penetration depth which is much shorter than the film thickness, so that

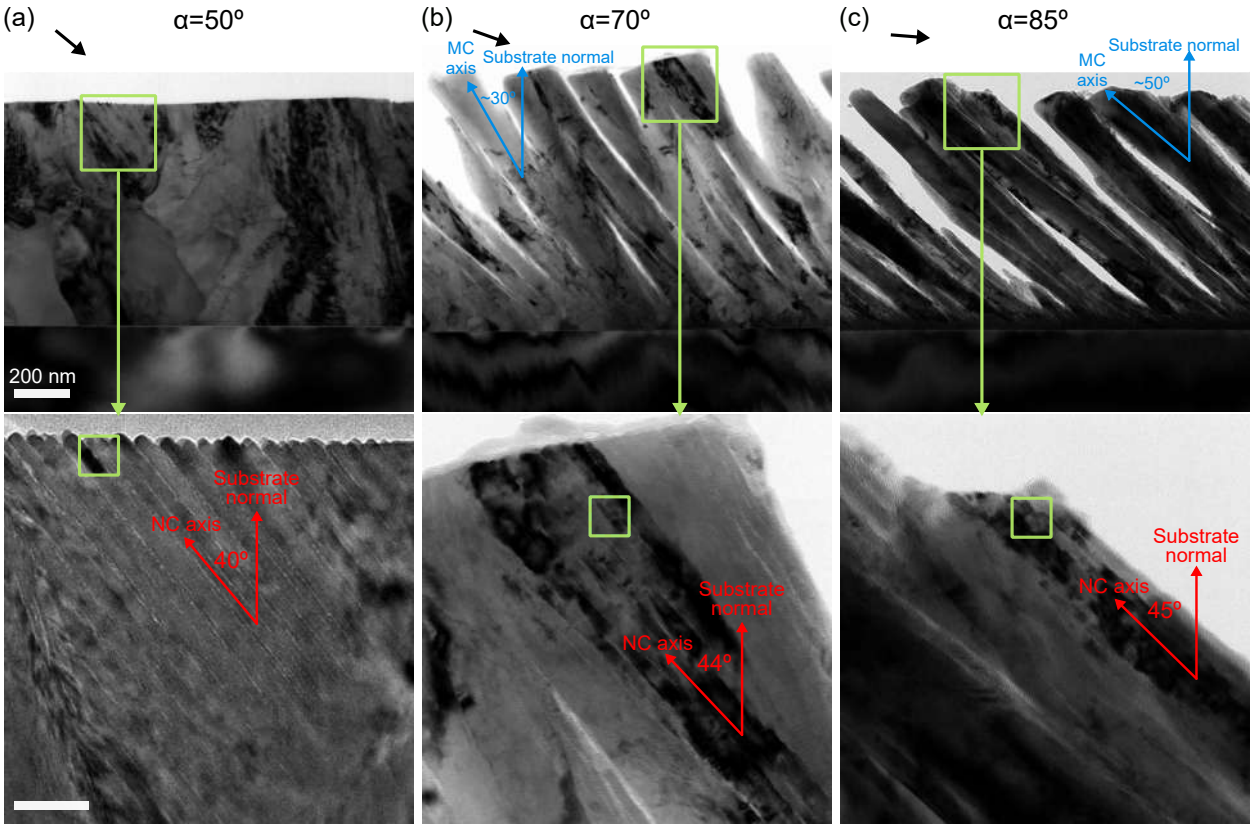

Figure 6: Bright-field TEM micrograph of the ITO films deposited with Xe at different angles: (a) $\alpha = 50\,^{\circ}$, (b) $\alpha = 70\,^{\circ}$ and (c) $\alpha = 85\,^{\circ}$. General views (on top) and magnified views close to the surface (at the bottom), shown with the same scales, evidence the presence of nanoscopic columnar structures with similar tilt within the macroscopic columns. The black arrows depicted at the surface of the coatings indicate the direction of the incoming deposition flux.

SE measurements only probes typically the first top $\sim$ 100 nm of the ITO film. This can be easily verified by simulating the transmitted intensity with the above mentioned model, which becomes negligible for films thicker than $\sim$ 200 nm (this length then has to be divided by 2 for the reflected light since it needs to go back and forth at least once). Therefore, the ABEMA model used in the Visible-NIR range, which takes into account the porous and tilted columnar structure of the total thickness of the film, although in principle still valid, is no longer the dominating source of anisotropy, and we should consider a model reproducing the optical properties of the first few tens of nanometers at the top of the film instead.

Understanding the optical anisotropy in the IR range for the ITO films prepared with Xe is far from being straightforward. Nevertheless, some answers can be found by taking a closer look to the film nanostructure close to the surface. According to the bright-field TEM micrographs (Fig. 6), we actually observe a sub-columnar structure which appears as a bundle of nanoscopic columns (NC) parallel to one another. Those NC structures are sparingly and locally distributed at the surface of the film deposited with $\alpha = 50\,^{\circ}$ (Fig. 6(a)), whereas they are more dominant within each macroscopic columns (MC) when the deposition angle is increased to $70\,^{\circ}$ (Fig. 6(b)) and $85\,^{\circ}$ (Fig. 6(c)) for instance. Those NCs are highly elongated and roughly tilted towards the deposition flux (their width is typically of a few nanometers, while their length is few tens of nanometers). Interestingly, we notice that while the tilt of the MC (β) raises with α ($\beta \approx 30\,^{\circ}$ for $\alpha = 70\,^{\circ}$, $\beta \approx 50\,^{\circ}$ for $\alpha = 85\,^{\circ}$, as expected for OAD films), the NC tilt relative to the substrate normal (β_{NC}) remains constant (about $40 - 45\,^{\circ}$) and is almost independent of the deposition angle.

High-Resolution TEM (HRTEM) micrographs (Fig. 7) were acquired in smaller areas to know the crystallinity of the NCs structures: they are found pretty well crystallized in their core, while the boundaries be-

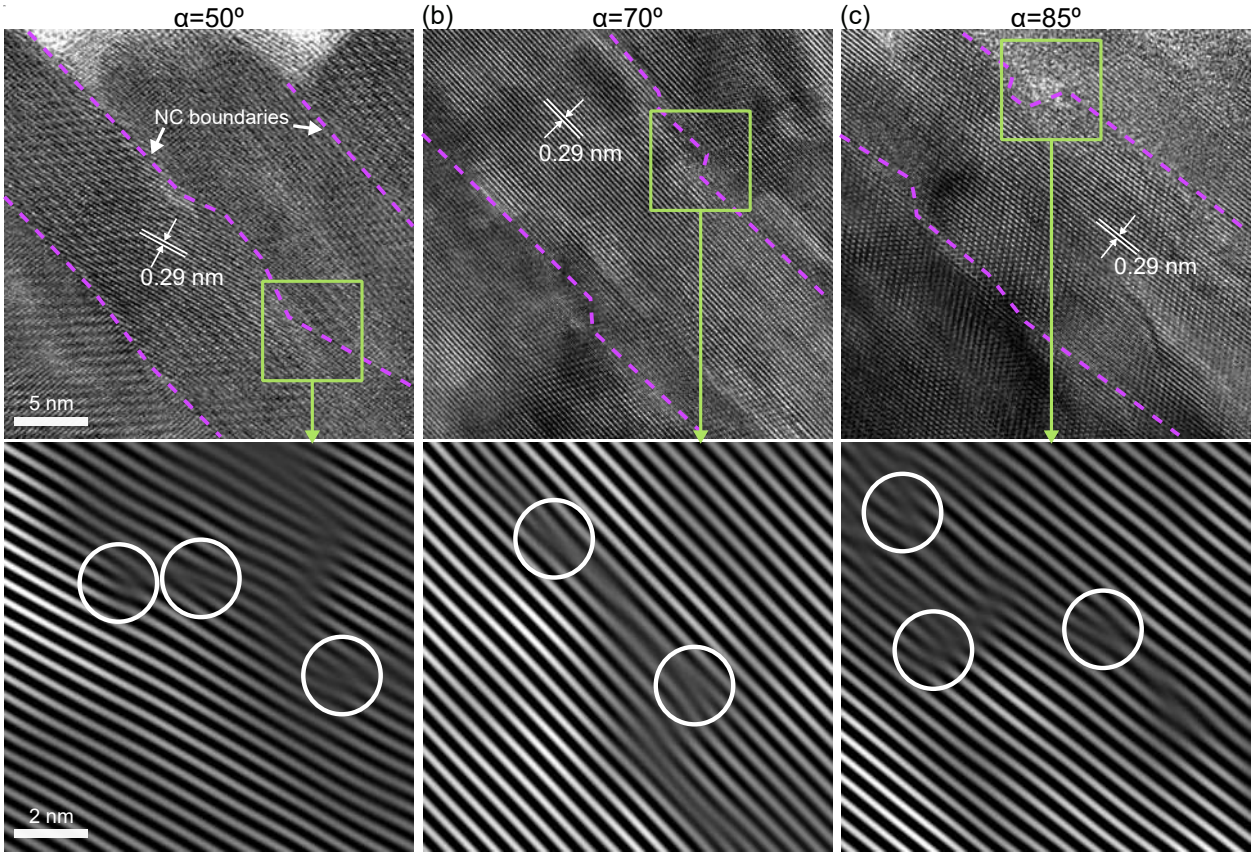

Figure 7: HRTEM micrograph of the ITO films deposited with Xe at different angles: (a) $\alpha = 50\,^\circ$, (b) $\alpha = 70\,^\circ$ and (c) $\alpha = 85\,^\circ$. These micrographs where taken in the NCs regions indicated by green squares in the bottom images of Fig. 6. The bottom images show filtered micrographs obtained using the planes at the vicinity limit between two NCs. Crystal discontinuities are highlighted by white circles.

tween neighboring NCs appears more disturbed. On all the images, we clearly see reticular planes with distances of 0.29 nm, which is typical of {222} planes of the cubic bixbyite (C-type) structure of In_2O_3 (although, we mention here that the Rh phase cannot be discarded neither). Using those planes to filter the HRTEM images, we can clearly see the presence of crystal discontinuities at the border of the NCs that may be attributed to the presence of dislocations and grain boundaries.

Those NC structures may provide reasonable explanations concerning the evolutions of the θ_{IR} angle and μ_2 mobilities. (i) First, the tilt of the nanocolumns is almost constant with deposition angle: $\beta_{NC} \approx 40 - 45\,^\circ$ whatever α is, which correlates nicely with the convergence of the θ_{IR} values to $\approx 50 - 55\,^\circ$ for $\alpha \geq 60\,^\circ$. Despite somewhat different, these values are close to one another: one may recall that they are obtained from very distinct experimental techniques, namely TEM and IR Ellipsometry. It is highly striking that both β_{NC} and θ_{IR} are independent of α, since all other structural parameters, such as the column tilt angle β and the porosity, depend strongly on the deposition angle. The θ_{IR} increases for α below $60 - 65\,^\circ$ could be explained by the fact that NCs arrangements are in minority for $\alpha = 50\,^\circ$ and tend to develop further at higher α. (ii) Secondly, the morphology of the NCs structures (elongated along the c direction and very thin along the b axis) and their crystallinity (cores without defects but presence of defective boundaries) could explain nicely the drop of μ_{2b}, while $\mu_{2a,c}$ remains almost unchanged, as detailed in the next paragraph. Understanding finely the development of such NC structures is a crucial and exciting research topic but is beyond the scope of this paper. Another work dealing with the texture evolution in such systems is currently in progress as we expect that changes in preferential crystalline orientation of obliquely deposited ITO films, as already pointed out in Ref. [25], may trigger the formation of such atypical nanoscale features that can have strong effects on the optical and electrical properties.

We may now discuss the connection between the NCs structure and the IR optical anispotropy. For transparent conductive oxides (TCOs) in general, it is usually claimed that optical measurements in the visible or IR range probes the in-grain properties [60, 61, 62, 63]. In the metallic regime below the free carrier absorption edge, under the excitation of an electromagnetic field of frequency ν the electrons (or holes) endure a collective excitation (plasma oscillations) by oscillating back and forth with a spatial amplitude l typically of the order of $l = v_F/2\nu$, where v_F is the Fermi velocity. For the Xe film at $\alpha = 85\,^\circ$ for example, with a carrier density of $N_e = 3.4\,10^{20}\,\mathrm{e.cm^{-3}}$, by assuming a parabolic band profile with an effective mass of $m_* = 0.35$ the Fermi velocity is $v_F = 7.1\,10^5\,\mathrm{m.s^{-1}}$, so that for example $l = 2\,\mathrm{nm}$ at a wavelength of $\lambda = 1.7\,\mu\mathrm{m}$, the onset of the free-carrier-driven optical behavior for Xe films. For most TCOs films reported, l is commonly way smaller than the mean crystalline grain size, which is typically few tens of nanometers. Therefore, the mobility as extracted from the Drude model represents the in-grain mobility, due to intrinsic scattering phenomena such as ionized impurity scattering, electron-phonon collisions, and so on. On the other hand, the mobility measured by DC electrical measurements (resistivity and Hall effect) includes the effects of grain boundary scattering. In our ITO films, in the IR range, l is indeed way smaller than the grain size (few tens of nanometers) in the direction parallel to the NCs, but this is not the case for the direction perpendicular to the NCs, which have a typical width of $\approx 10\,\mathrm{nm}$, as can be seen in Figure 7. Therefore, the mobility in the b direction is strongly reduced ($\mu_{2b} \approx 3\,\mathrm{cm^2.V^{-1}.s^{-1}}$) compared to the one in the a and c directions ($\mu_{2a,c} \approx 12\,\mathrm{cm^2.V^{-1}.s^{-1}}$) because it is limited by electron scattering at the grain boundaries between the NCs, while $\mu_{2a,c}$ indeed represent the in-grain mobility.

This sub-columnar structure is evidenced by transmission electron microscopy for the Xe (Figures 6 and 7), but it is absent in the Ar films, which explains why IR optical anisotropy is not observed in their case. As pointed out in a previous paper [25], the Ar films are indeed less crystalline than the Xe ones, which is why the nanocolumns are not allowed to grow coherently on a sufficiently long length scale to be observable. The size of the crystalline grains is significantly smaller for the Ar films, and the mobility is consequently reduced to $\mu_{2,\mathrm{Ar}} = 6\,\mathrm{cm^2.V^{-1}.s^{-1}}$ at $\alpha = 85\,^\circ$. This low value is approaching the lowest mobility for the Xe films, $\mu_{2b} \approx 3\,\mathrm{cm^2.V^{-1}.s^{-1}}$.

We may therefore conclude that the optical anisotropy in the IR range stems from the sub-columnar structure of the OAD macroscopic columns. Such a biaxial Drude model is commonly used in the literature for anisotropic crystals, like e.g. $Mg(B_{1-x}C_x)_2$ [64] or cuprates [65], and is also applied to strongly anisotropic nanostructures like e.g. carbon nanotubes in the terahertz region [66]. It is, however, quite original to apply it to an isotropic material like ITO enduring nanostructuration. We suggest that this biaxial Drude model may be of a great help to model the anisotropic optical properties of metallic OAD nanostructured films, for which such a sub-columnar structure appears to be a general trend, as pointed out recently by Beainou et al. [67].

5. Conclusion

In this paper, we investigated the optical properties of OAD ITO films grown by ion beam sputtering by the mean of Mueller matrices spectroscopic ellipsometry, and correlated them to the nanostructure investigated by HRTEM.

In the visible range, the measured MM elements are well reproduced by a two-layer model: the first (thin) seed layer is dense, and the second (porous) layer is well described by the mean of an Anisotropic Bruggeman Effective Medium Approximation. The porosity quantified from this model is found to be significantly higher in ITO films when Xe ions are used to sputter the target (porosity of up to 50 %) rather than Ar ones (up to 30 %). We evidence a strong anisotropy of the optical properties, with a biaxial structure. The principal axes are tilted within the slanting plane of the nanocolumns, and this tilt angle θ_{vis} is shown to coincide with the slanting angle of the columns β. The optical index is maximum in the direction a perpendicular to the slanting plane, due to the lateral percolation of the nanocolumns generating a ripple-like structure in the direction perpendicular to the incident matter flux. This feature appears to be a unique footprint of IBS deposition: indeed, OAD films commonly deposited by electron beam evaporation such as SiO_2 [46] or Co, Ti and Si [36] usually have higher optical index in the direction c parallel to the nanocolumns, and not along the axis a like our IBS films do.

The birefringence projected in the sample plane Δn also shows a dependence on the nature of the impinging ion. For the Xe-deposited films, which are more porous, Δn first increases with the deposition angle α, and reaches a maximum value of 0.05 before collapsing for higher α values. This is a common behavior for OAD dielectric films [49, 26, 50, 51, 52], resulting from a competition between increasing birefringence induced

by the columnar structure, and an overall lowering of the optical indices due to the porosity [53, 54, 55]. On the contrary, this downturn is not observed in the Ar films, probably because their porosity is never high enough to balance the increase of birefringence.

In the infrared range, there is a sharp difference between the two types of ions. For the Ar-deposited films, the optical properties are well reproduced by the ABEMA model used for the visible range, giving rise to almost negligible anisotropy in the IR, due to the low level of porosity ($< 30\,\%$). On the contrary, the Xe films exhibit strongly anisotropic optical properties, which cannot be explained by an ABEMA model. We showed that a biaxial Drude model reproduces quite well the optical properties, due to the presence of nanocolumns inside the macroscopic columns: the scattering probed by the IR light is limited by grain boundary scattering at the nanometer scale, and thus strongly reduced, in the direction perpendicular to the nanocolumn, while it indeed corresponds to the in-grain scattering in the directions parallel to it. This biaxial Drude model, and the underlying anisotropic scattering mechanisms, are quite original, and may be applicable to other OAD conducting films exhibiting similar sub-columnar structure.

These results highlight the potential of IBS combined with OAD to manufacture ITO films with original and adjustable characteristics. The choice of the impinging ion (Ar or Xe) allows to reach and to finely tune a wide range of optical properties, including lowered optical indices (control of the porosity), birefringence in the visible range (control of the downturn of Δn), and birefringence in the infrared range (present or not). It can also be envisioned as a suitable bottom-up fabrication technique for large scale production of anisotropic transparent conducting thin films.

More generally, this work presents a thorough study of the anisotropic optical properties of transparent and conducting thin films in both visible and infrared ranges, which are generally overlooked because of the difficulty to characterize them, despite their paramount importance in numerous applications such as retarders or high-transmittance polarizers. While studies of the anisotropic optical properties of dielectric or highly porous metallic metamaterials made e.g. by OAD have been reported, this works fills a gap in the available literature for transparent and conducting films with intermediate porosity, by proposing a reliable method relying on a carefully confrontation of HRTEM results and optical measurements, and on the development of advanced optical models.

References

[1] J.-Q. Xi, M. F. Schubert, J. K. Kim, E. F. Schubert, M. Chen, S.-Y. Lin, W. Liu, J. A. Smart, Optical thin-film materials with low refractive index for broadband elimination of fresnel reflection, Nature photonics 1 (3) (2007) 176.

[2] F. Maudet, B. Lacroix, A. J. Santos, F. Paumier, M. Paraillous, S. Hurand, A. Corvisier, C. Dupeyrat, R. García, F. M. Morales, et al., On the importance of light scattering for high performances nanostructured antireflective surfaces, Acta Materialia 188 (2020) 386–393.

[3] F. Maudet, B. Lacroix, A. Santos, F. Paumier, M. Paraillous, C. Dupeyrat, R. García, F. Morales, T. Girardeau, Towards perfect mwir transparency using oblique angle deposition, Applied Surface Science 470 (2019) 943–950.

[4] D. Schmidt, B. Booso, T. Hofmann, E. Schubert, A. Sarangan, M. Schubert, Monoclinic optical constants, birefringence, and dichroism of slanted titanium nanocolumns determined by generalized ellipsometry, Applied Physics Letters 94 (1) (2009) 011914.

[5] R. Latz, K. Michael, M. Scherer, High conducting large area indium tin oxide electrodes for displays prepared by dc magnetron sputtering, Japanese journal of applied physics 30 (2A) (1991) L149.

[6] M. Sawada, M. Higuchi, S. Kondo, H. Saka, Characteristics of indium-tin-oxide/silver/indium-tin-oxide sandwich films and their application to simple-matrix liquid-crystal displays, Japanese Journal of Applied Physics 40 (5R) (2001) 3332.

[7] X. Yan, F. W. Mont, D. J. Poxson, M. F. Schubert, J. K. Kim, J. Cho, E. F. Schubert, Refractive-index-matched indium–tin-oxide electrodes for liquid crystal displays, Japanese Journal of Applied Physics 48 (12R) (2009) 120203.

[8] H. Kim, A. Pique, J. Horwitz, H. Mattoussi, H. Murata, Z. Kafafi, D. Chrisey, Indium tin oxide thin films for organic light-emitting devices, Applied physics letters 74 (23) (1999) 3444–3446.

[9] H. Kim, a. C. Gilmore, A. Pique, J. Horwitz, H. Mattoussi, H. Murata, Z. Kafafi, D. Chrisey, Electrical, optical, and structural properties of indium–tin–oxide thin films for organic light-emitting devices, Journal of Applied Physics 86 (11) (1999) 6451–6461.

[10] J. K. Kim, T. Gessmann, E. F. Schubert, J.-Q. Xi, H. Luo, J. Cho, C. Sone, Y. Park, Gainn light-emitting diode with conductive omnidirectional reflector having a low-refractive-index indium-tin oxide layer, Applied physics letters 88 (1) (2006) 013501.

[11] I. Hamberg, C. G. Granqvist, Evaporated sn-doped in2o3 films: Basic optical properties and applications to energy-efficient windows, Journal of Applied Physics 60 (11) (1986) R123–R160.

[12] G. Oh, E. K. Kim, Antireflection coatings with graded refractive index of indium tin oxide for si-based solar cells, Journal of the Korean Physical Society 74 (2) (2019) 127–131.

[13] J. W. Leem, J. S. Yu, Glancing angle deposited ito films for efficiency enhancement of a-si: H/μc-si: H tandem thin film solar cells, Optics express 19 (103) (2011) A258–A269.

[14] P. Topart, P. Hourquebie, Infrared switching electroemissive devices based on highly conducting polymers, Thin Solid Films 352 (1-2) (1999) 243–248.

[15] M. Siddiqui, A. Saxena, S. Singh, Deposition and characterization of ito thin film over glass for defogger application and for solar photovoltaics (2018).

[16] H. Löbl, M. Huppertz, D. Mergel, Ito films for antireflective and antistatic tube coatings prepared by dc magnetron sputtering, Surface and Coatings Technology 82 (1-2) (1996) 90–98.

[17] J.-Y. Kwon, D.-J. Lee, K.-B. Kim, Transparent amorphous oxide

semiconductor thin film transistor, Electronic Materials Letters 7 (1) (2011) 1–11.
[18] B. G. Lewis, D. C. Paine, Applications and processing of transparent conducting oxides, MRS bulletin 25 (8) (2000) 22–27.
[19] A. Dawar, J. Joshi, Semiconducting transparent thin films: their properties and applications, Journal of Materials Science 19 (1) (1984) 1–23.
[20] C. Granqvist, Transparent conductive electrodes for electrochromic devices: A review, Applied Physics A 57 (1) (1993) 19–24.
[21] Z. Ma, Z. Li, K. Liu, C. Ye, V. J. Sorger, Indium-tin-oxide for high-performance electro-optic modulation, Nanophotonics 4 (2) (2015) 198–213.
[22] K. Ellmer, Past achievements and future challenges in the development of optically transparent electrodes, Nature Photonics 6 (12) (2012) 809–817.
[23] A. Boileau, S. Hurand, F. Baudouin, U. Lüders, M. Dallocchio, B. Bérini, A. Cheikh, A. David, F. Paumier, T. Girardeau, et al., Highly transparent and conductive indium-free vanadates crystallized at reduced temperature on glass using a 2d transparent nanosheet seed layer, Advanced Functional Materials (2021) 2108047.
[24] P. Guo, R. P. Chang, R. D. Schaller, Tunable infrared hyperbolic metamaterials with periodic indium-tin-oxide nanorods, Applied Physics Letters 111 (2) (2017) 021108.
[25] B. Lacroix, A. J. Santos, S. Hurand, A. Corvisier, F. Paumier, T. Girardeau, F. Maudet, C. Dupeyrat, R. Garcia, F. M. Morales, Nanostructure and physical properties control of indium tin oxide films prepared at room temperature through ion beam sputtering deposition at oblique angles, The Journal of Physical Chemistry C (2019).
[26] K. D. Harris, A. C. van Popta, J. C. Sit, D. J. Broer, M. J. Brett, A birefringent and transparent electrical conductor, Advanced Functional Materials 18 (15) (2008) 2147–2153.
[27] D. U. Yildirim, A. Ghobadi, M. C. Soydan, O. Atesal, A. Toprak, M. D. Caliskan, E. Ozbay, Disordered and densely packed ito nanorods as an excellent lithography-free optical solar reflector metasurface, ACS Photonics (2019).
[28] D. J. Poxson, F. W. Mont, M. F. Schubert, J. K. Kim, E. F. Schubert, Quantification of porosity and deposition rate of nanoporous films grown by oblique-angle deposition, Applied Physics Letters 93 (10) (2008) 101914.
[29] Y. Zhong, Y. Shin, C. Kim, B. Lee, E. Kim, Y. Park, K. Sobahan, C. Hwangbo, Y. Lee, T. G. Kim, Optical and electrical properties of indium tin oxide thin films with tilted and spiral microstructures prepared by oblique angle deposition, Journal of Materials Research 23 (9) (2008) 2500–2505.
[30] K. Kim, J. H. Park, H. Kim, J. K. Kim, E. Fred Schubert, J. Cho, Energy bandgap variation in oblique angle-deposited indium tin oxide, Applied Physics Letters 108 (4) (2016) 041910.
[31] D. Kim, Y. Han, J.-S. Cho, S.-K. Koh, Low temperature deposition of ito thin films by ion beam sputtering, Thin Solid Films 377 (2000) 81–86.
[32] Y. Han, D. Kim, J.-S. Cho, S.-K. Koh, Y. S. Song, Tin-doped indium oxide (ito) film deposition by ion beam sputtering, Solar energy materials and solar cells 65 (1-4) (2001) 211–218.
[33] C. Bundesmann, J. Bauer, A. Finzel, J. W. Gerlach, W. Knolle, A. Hellmich, R. Synowicki, Properties of indium tin oxide thin films grown by ar ion beam sputter deposition, Journal of Vacuum Science & Technology A: Vacuum, Surfaces, and Films 39 (3) (2021) 033406.
[34] F. Maudet, B. Lacroix, A. J. Santos, F. Paumier, M. Paraillous, S. Hurand, A. Corvisier, C. Marsal, B. Giroire, C. Dupeyrat, et al., Optical and nanostructural insights of oblique angle deposited layers applied for photonic coatings, Applied Surface Science 520 (2020) 146312.
[35] O. Arteaga, Useful mueller matrix symmetries for ellipsometry, Thin Solid Films 571 (2014) 584–588.
[36] D. Schmidt, M. Schubert, Anisotropic bruggeman effective medium approaches for slanted columnar thin films, Journal of Applied Physics 114 (8) (2013) 083510.
[37] Y. S. Jung, Spectroscopic ellipsometry studies on the optical constants of indium tin oxide films deposited under various sputtering conditions, Thin Solid Films 467 (1-2) (2004) 36–42.
[38] D. Liang, D. Schmidt, H. Wang, E. Schubert, M. Schubert, Generalized ellipsometry effective medium approximation analysis approach for porous slanted columnar thin films infiltrated with polymer, Applied Physics Letters 103 (11) (2013) 111906.
[39] M. Losurdo, K. Hingerl, Ellipsometry at the Nanoscale, Springer, 2013.
[40] R. Bilboul, A note on the permittivity of a double-layer ellipsoid, Journal of Physics D: Applied Physics 2 (6) (1969) 921.
[41] S. Berthier, Anisotropic effective medium theories, Journal de Physique I 4 (2) (1994) 303–318.
[42] V. D. Bruggeman, Berechnung verschiedener physikalischer konstanten von heterogenen substanzen. i. dielektrizitätskonstanten und leitfähigkeiten der mischkörper aus isotropen substanzen, Annalen der physik 416 (7) (1935) 636–664.
[43] J. Nieuwenhuizen, H. Haanstra, Microfractography of thin films, Philips Tech Rev 27 (3) (1966) 87–91.
[44] R. Tait, T. Smy, M. Brett, Modelling and characterization of columnar growth in evaporated films, Thin Solid Films 226 (2) (1993) 196–201.
[45] S. Lichter, J. Chen, Model for columnar microstructure of thin solid films, Physical review letters 56 (13) (1986) 1396.
[46] F. Maudet, Nanostructured layers by oblique incidence deposition : Microstructure and optical properties correlations applicated to high-performance anti-reflection treatments in extended visible and infrared range, Ph.D. thesis (2018).
[47] A. W. Sood, D. J. Poxson, F. W. Mont, S. Chhajed, J. Cho, E. F. Schubert, R. E. Welser, N. K. Dhar, A. K. Sood, Experimental and theoretical study of the optical and electrical properties of nanostructured indium tin oxide fabricated by oblique-angle deposition, Journal of nanoscience and nanotechnology 12 (5) (2012) 3950–3953.
[48] C.-G. Granqvist, O. Hunderi, Optical properties of ultrafine gold particles, Physical Review B 16 (8) (1977) 3513.
[49] M. M. Hawkeye, M. T. Taschuk, M. J. Brett, Glancing angle deposition of thin films: engineering the nanoscale, John Wiley & Sons, 2014.
[50] S. Wang, G. Xia, X. Fu, H. He, J. Shao, Z. Fan, Preparation and characterization of nanostructured zro2 thin films by glancing angle deposition, Thin Solid Films 515 (7-8) (2007) 3352–3355.
[51] J. Gospodyn, J. Sit, Characterization of dielectric columnar thin films by variable angle mueller matrix and spectroscopic ellipsometry, Optical Materials 29 (2-3) (2006) 318–325.
[52] S. Wang, G. Xia, H. He, K. Yi, J. Shao, Z. Fan, Structural and optical properties of nanostructured tio2 thin films fabricated by glancing angle deposition, Journal of Alloys and Compounds 431 (1-2) (2007) 287–291.
[53] I. Hodgkinson, Q. H. Wu, S. Collett, Dispersion equations for vacuum-deposited tilted-columnar biaxial media, Applied optics 40 (4) (2001) 452–457.
[54] W. Jian-Guo, S. Jian-Da, F. Zheng-Xiu, Effective medium model for refractive indices of thin films with oblique columnar structure, Chinese Physics Letters 22 (1) (2005) 221.
[55] W. Jian-Guo, S. Jian-Da, W. Su-Mei, H. Hong-Bo, F. Zheng-Xiu, Form birefringence in thin films with oblique columnar structures, Chinese Physics Letters 22 (8) (2005) 2066.
[56] G. Mbise, D. Le Bellac, G. Niklasson, C. Granqvist, Angular

selective window coatings: theory and experiments, Journal of Physics D: Applied Physics 30 (15) (1997) 2103.
[57] D. Schmidt, B. Booso, T. Hofmann, E. Schubert, A. Sarangan, M. Schubert, Generalized ellipsometry for monoclinic absorbing materials: determination of optical constants of cr columnar thin films, Optics letters 34 (7) (2009) 992–994.
[58] D. Schmidt, Generalized ellipsometry on sculptured thin films made by glancing angle deposition, Ph.D. thesis (2010).
[59] M. Mansour, A.-S. Keita, B. Gallas, J. Rivory, A. Besnard, N. Martin, Optical anisotropy of tilted columns thin films of chromium deposited at oblique incidence, Optical Materials 32 (9) (2010) 1146–1153.
[60] J. Steinhauser, S. Fay, N. Oliveira, E. Vallat-Sauvain, C. Ballif, Transition between grain boundary and intragrain scattering transport mechanisms in boron-doped zinc oxide thin films, Applied Physics Letters 90 (14) (2007) 142107.
[61] H. Fujiwara, M. Kondo, Effects of carrier concentration on the dielectric function of zno:ga and in2o3:sn studied by spectroscopic ellipsometry: analysis of free-carrier and band-edge absorption, Physical Review B 71 (7) (2005) 075109.
[62] T. Yamada, H. Makino, N. Yamamoto, T. Yamamoto, Ingrain and grain boundary scattering effects on electron mobility of transparent conducting polycrystalline ga-doped zno films, Journal of Applied Physics 107 (12) (2010) 123534.
[63] N. Ehrmann, R. Reineke-Koch, Ellipsometric studies on zno:al thin films: Refinement of dispersion theories, Thin Solid Films 519 (4) (2010) 1475–1485.
[64] T. Kakeshita, S. Lee, S. Tajima, Anisotropic drude response and the effect of anisotropic c substitution in mg(b1-xcx)2, Physical review letters 97 (3) (2006) 037002.
[65] M. Dumm, S. Komiya, Y. Ando, D. Basov, Anisotropic electromagnetic response of lightly doped la2-xsrxcuo4 within the cuo2 planes, Physical review letters 91 (7) (2003) 077004.
[66] T.-I. Jeon, K.-J. Kim, C. Kang, I. H. Maeng, J.-H. Son, K. H. An, J. Y. Lee, Y. H. Lee, Optical and electrical properties of preferentially anisotropic single-walled carbon-nanotube films in terahertz region, Journal of Applied Physics 95 (10) (2004) 5736–5740.
[67] R. El Beainou, A. Garcia-Valenzuela, M. Raschetti, J.-M. Cote, R. Alvarez, A. Palmero, V. Potin, N. Martin, A 4-view imaging to reveal microstructural differences in obliquely sputter-deposited tungsten films, Materials Letters 264 (2020) 127381.

Highlights

Anisotropic optical properties of indium tin oxide thin films prepared by ion beam sputtering under oblique angle deposition

Simon Hurand, Alan Corvisier, Bertrand Lacroix, Antonio Jesús Santos, Florian Maudet, Cyril Dupeyrat, Rafael García Roja, Francisco Miguel Morales, Thierry Girardeau, Fabien Paumier

- Anisotropic optical properties of ITO nanostructures grown by IBS-OAD are addressed
- Mueller matrix Vis-NIR and IR spectroscopic ellipsometry is implemented
- Models validated by HRTEM allow describing the strong anisotropies in both ranges
- A ripple-like structure normal to the deposition flux is responsible for Vis-NIR anisotropy
- Free-carrier scattering in nanoscopic sub-columnar structures causes IR anisotropy

Graphical Abstract

Anisotropic optical properties of indium tin oxide thin films prepared by ion beam sputtering under oblique angle deposition

Simon Hurand, Alan Corvisier, Bertrand Lacroix, Antonio Jesús Santos, Florian Maudet, Cyril Dupeyrat, Rafael García Roja, Francisco Miguel Morales, Thierry Girardeau, Fabien Paumier